



Cite this: *Nanoscale*, 2025, **17**, 11385

## Nano-bismuth vanadate supported on fibrous silica reduces the intrinsic charge impedance for superior photoelectrochemical water-splitting performance†

N. M. Izzudin, <sup>a</sup> A. A. Jalil, <sup>\*a,b,c</sup> Saravanan Rajendran, <sup>d</sup> N. S. Hassan, <sup>b</sup> M. H. Sawal, <sup>a</sup> N. I. H. Hazril, <sup>a</sup> Y. Nagao, <sup>e</sup> K. Aoki <sup>e</sup> and S. H. Zein <sup>f</sup>

Bismuth vanadate ( $\text{BiVO}_4$ ) is one of the top-notch materials used in photoelectrochemical (PEC) water-splitting studies owing to its promising properties. However, its practical application is significantly hindered by its inherent limitations, which reduce its efficiency in water-splitting processes. In this study, a novel approach involving size transformation and improved dispersion of  $\text{BiVO}_4$  was achieved via a micro-emulsion method, with fibrous silica serving as a support matrix. The fabricated catalyst, fibrous silica bismuth vanadate (FSBVO), was comprehensively characterized using XRD, FTIR, FESEM, TEM, UV-Vis/DRS, Mott–Schottky analysis, EIS, and PL spectroscopy and compared with commercial  $\text{BiVO}_4$ . The PEC analysis demonstrated that the FSBVO photoanode delivered a remarkable performance, attaining a photocurrent density of  $19.8 \text{ mA cm}^{-2}$  at  $1.23 \text{ V}_{\text{RHE}}$  and a solar-to-hydrogen conversion efficiency of 24.35%, which correspond to enhancements of approximately 27.5 and 27.4 times, respectively, compared with those obtained using the pristine  $\text{BiVO}_4$  photoanode. Further in-depth studies revealed that the improvement in the PEC water-splitting performance was mainly attributed to the transformation of  $\text{BiVO}_4$  into nanoparticles and the distinctive Si–Bi interaction, which increased the carrier density and facilitated efficient electron transport, thereby accelerating the oxygen evolution kinetics. This study highlights the potential of FSBVO photoanodes and provides valuable insights for designing advanced materials to enhance the PEC water-splitting efficiency.

Received 6th December 2024,  
Accepted 2nd April 2025

DOI: 10.1039/d4nr05153j  
[rsc.li/nanoscale](http://rsc.li/nanoscale)

### 1.0 Introduction

The excessive reliance on fossil fuels has led to severe environmental degradation and erratic climate change over the years.<sup>1,2</sup> These urgent issues have driven significant efforts toward developing and utilizing renewable energy sources. Among the myriad of alternatives under consideration, hydro-

gen has emerged as the focus of interest owing to its exceptional energy density surpassing those of the traditional fossil fuels, sustainability, and inherently eco-friendly attributes.<sup>3</sup> Among other hydrogen production strategies, photoelectrochemical (PEC) water splitting has emerged as a highly promising approach for generating renewable hydrogen. This method is particularly advantageous as carbon-related byproducts are not produced, thereby supporting the transition to a clean energy economy.<sup>3,4</sup> Given its unique attributes, PEC water splitting has been considered the “holy grail” of solar energy conversion and storage. It is widely recognized as a key technology for achieving the net-zero carbon emission targets by 2050 as outlined in the Paris Agreement.<sup>5–7</sup>

Generally, PEC water-splitting is a semiconductor-assisted process that utilizes the abundant and renewable energy of sunlight to split water molecules into hydrogen and oxygen.<sup>8,9</sup> As the oxygen evolution reaction (OER), which involves a four-electron process, is the rate-determining step in PEC water-splitting, designing efficient photoanode materials is the core challenge in this field.<sup>10–12</sup> An ideal photoanode material should exhibit several key properties, including high stability

<sup>a</sup>Faculty of Chemical and Energy Engineering, Universiti Teknologi Malaysia, 81310 UTM Johor Bahru, Johor, Malaysia. E-mail: r-aishahj@utm.my; Fax: +60-7-5536165; Tel: +60-7-5535581

<sup>b</sup>Centre of Hydrogen Energy, Institute of Future Energy, 81310 UTM Johor Bahru, Johor, Malaysia

<sup>c</sup>Chemical Engineering Department, Institut Teknologi Sepuluh Nopember, Kampus ITS Sukolilo, Surabaya 60111, Indonesia

<sup>d</sup>Instituto de Alta, Investigación, Universidad de Tarapacá, Arica-1000000, Chile

<sup>e</sup>School of Materials Science, Japan Advanced Institute of Science and Technology, 1-1 Asahidai, Nomi, Ishikawa 923-1211, Japan

<sup>f</sup>School of Engineering, Faculty of Science and Engineering, University of Hull, Kingston Upon Hull, UK

† Electronic supplementary information (ESI) available. See DOI: <https://doi.org/10.1039/d4nr05153j>

under operational conditions, strong light absorption, efficient charge transport, and adequate band edge position to overcome the energy barrier for OER.<sup>13,14</sup> Since the groundbreaking work by Fujishima and Honda in the early 1970s, which unveiled the potential of photo-assisted electrochemical water oxidation utilizing n-type  $\text{TiO}_2$  single-crystal electrodes, extensive research has been conducted on a diverse array of semiconductor materials, including  $\text{TiO}_2$ ,  $\text{ZnO}$ ,  $\text{Fe}_2\text{O}_3$ ,  $\text{WO}_3$ ,  $\text{BiVO}_4$ , and  $\text{Ga}_2\text{O}_3$ , as photoelectrodes for advancing PEC water-splitting technologies.<sup>15–19</sup> Despite their potential, these materials have significant limitations, including wide bandgap energy, low surface area, poor charge carrier mobility, and high rates of electron–hole recombination. These challenges hinder their scalability and practical application in industrial PEC systems.<sup>2,19</sup>

In recent years, bismuth vanadate ( $\text{BiVO}_4$ ) has garnered significant attention as a highly promising photoanode material for PEC water-splitting owing to its exceptional intrinsic attributes. These features include a theoretical photocurrent density of  $7.5 \text{ mA cm}^{-2}$  at  $1.23 \text{ V}_{\text{RHE}}$ , solar-to-hydrogen (STH) efficiency of 9.2%, narrow bandgap energy of 2.4 eV, optimal band edge alignment, environmental benignity, and remarkable photostability.<sup>1,20</sup> In 2022, Zhang *et al.* achieved a photocurrent density of  $0.61 \text{ mA cm}^{-2}$  by utilizing commercial  $\text{BiVO}_4$  under simulated sunlight in a  $0.2 \text{ M Na}_2\text{SO}_4$  electrolyte. Likewise, Meng *et al.* applied a spin-coating technique to produce  $\text{BiVO}_4$  photoanodes, achieving a photocurrent density of approximately  $0.68 \text{ mA cm}^{-2}$  in a  $1.0 \text{ M}$  phosphate buffer solution at pH 7.4.<sup>21</sup> However, despite these promising results,  $\text{BiVO}_4$ , similar to other semiconductor materials, cannot deliver a high STH efficiency for practical application due to its rapid carrier charge recombination and sluggish OER kinetics.<sup>15,22</sup>

Consequently, to mitigate this issue, various modifications of  $\text{BiVO}_4$  have been conducted. For instance, Hu *et al.* employed a chemical self-growth method to introduce an NiFe tannic acid (NFTA) complex and  $\text{Co(OH)}_2$  on the surface of  $\text{BiVO}_4$ . This dual OER cocatalyst showed enhanced interfacial charge separation, which boosted the photocurrent density ( $4.97 \text{ mA cm}^{-2}$ ).<sup>23</sup> Similarly, Dong *et al.* demonstrated that loading an NiFe-layered double hydroxide (LDH) OER cocatalyst onto  $\text{BiVO}_4$  not only enhanced its photocurrent density but also provided a protective layer, which substantially increased its resistance towards photo-corrosion.<sup>24</sup> In addition, nanosizing semiconductor particles is also a good approach for enhancing the accessibility to their active sites and improving their light absorption capacity and carrier density.<sup>25–27</sup> However, at smaller sizes, the quantum confinement effect can limit the electron mobility, thereby constraining the PEC performance of single semiconductor materials.<sup>28,29</sup> Thus, to mitigate this limitation, the incorporation of a suitable support material is essential when adopting this method.

Recently, spherical fibrous silica has been recognized as a highly favorable support material for PEC water-splitting applications, which is attributed to its remarkable physicochemical properties and structural advantages. These advantages include a high surface area, adjustable pore size, and excellent

chemical stability, which can collectively contribute to enhancing the PEC water-splitting efficiency.<sup>30,31</sup> Our research group previously developed several fibrous silica-based materials for PEC water-splitting. For instance, Sawal and co-workers recently investigated the synthesis of fibrous silica-titania (FST) *via* the microemulsion technique.<sup>32</sup> The resulting FST exhibited well-dispersed  $\text{TiO}_2$  on the fibrous silica matrix and an impressive photocurrent density of  $13.8 \text{ mA cm}^{-2}$  at  $1.23 \text{ V}_{\text{RHE}}$ , which significantly outperformed pure  $\text{TiO}_2$  ( $5.51 \text{ mA cm}^{-2}$ ).<sup>32</sup> Building on this success, Abdullah and colleagues employed the same synthesis method to develop fibrous silica-zinc (FSZn) for solar-driven water oxidation. The FSZn photoanode achieved an impressive photocurrent density of  $17.9 \text{ mA cm}^{-2}$ , exceeding that of commercial  $\text{ZnO}$  ( $6.28 \text{ mA cm}^{-2}$ ).<sup>33</sup> This exceptional performance is attributed to the conduction band position of FSZn, which is strategically aligned near the hydrogen evolution reaction potential, thereby enabling rapid and efficient charge transfer.

To the best of our knowledge, there have been no prior reports on the development of fibrous silica-bismuth vanadate (FSBVO) for PEC water splitting. Building on the insights from earlier studies, this work introduces a novel FSBVO photoanode designed for PEC water-splitting applications. Comprehensive characterization techniques, including XRD, FTIR, FESEM, TEM, UV-Vis/DRS, Mott–Schottky, EIS, and PL, were employed to evaluate the physicochemical, optical, and photoelectrochemical properties of both FSBVO and commercial  $\text{BiVO}_4$ . The remarkable PEC performance of FSBVO was attributed to the transformation of bulk  $\text{BiVO}_4$  into nanoparticles and the incorporation of the unique fibrous silica structure, which enhanced the light absorption and facilitated efficient charge carrier transfer. Through the integration of diverse characterization techniques and comprehensive data analysis, we proposed the detailed water-splitting mechanism, shedding light on the underlying fundamental processes for the enhanced PEC performance of FSBVO.

## 2.0 Experimental

### 2.1 Chemicals

Commercial bismuth vanadate ( $\text{BiVO}_4$ ) with 99% purity was purchased from Chem Scene Sdn. Bhd., Malaysia. Tetraethyl orthosilicate (TEOS), cetyltrimethylammonium bromide (CTAB), butanol ( $\text{BuOH}$ ) and toluene with 98%, 99%, 99.5% and 99.5% purity, respectively, were supplied by Merck Sdn. Bhd., Malaysia. Urea was obtained from Vchem Sdn. Bhd., Malaysia, whereas sodium sulfate ( $\text{Na}_2\text{SO}_4$ ) was bought from QReC Sdn. Bhd. and utilized as the electrolyte solution. The pH system was calibrated using HCl or NaOH solution dropwise.

### 2.2 Fabrication of photoanodes

$\text{BiVO}_4$  purchased from Chem Scene Sdn. Bhd. was used directly to prepare the  $\text{BiVO}_4$  photoanode. The preparation process involved two main steps, as follows: (1) synthesis of

photoanode material (catalyst) and (2) deposition of the catalyst on a fluorine-doped tin oxide (FTO) film.

**2.2.1 Fabrication of fibrous silica bismuth vanadate (FSBVO).** Fibrous silica bismuth vanadate (FSBVO) was successfully prepared *via* an *in situ* microemulsion technique, following the method outlined in a previous study, as shown in Fig. 1.<sup>34</sup> Importantly, commercial  $\text{BiVO}_4$  was used as the metal seed instead of  $\text{MoO}_3$ . Briefly, a perquisite amount of urea, water, and CTAB was mixed in a 2 L Teflon flask, and the resulting solution was vigorously stirred for 30 min to ensure uniform mixing. Afterward, toluene and butanol were introduced in the mixture in a 5 : 2 molar ratio and stirred continuously for 1 h. Subsequently, TEOS was added gradually dropwise to the reaction mixture, which was continuously stirred for 8 h at 423 K. The resulting solution was subjected to microwave irradiation at a power of 480 W for 2 h. Following this, the mixture was centrifuged to isolate a bright-yellow precipitate. The precipitate was thoroughly washed with acetone and distilled water, and then dried overnight at 403 K. The dried product was finely ground into a powder and underwent calcination in a muffle furnace at 853 K for 8 h at a controlled heating rate of 3 °C per min. The resulting product was placed in a sample bottle and labeled as FSBVO.

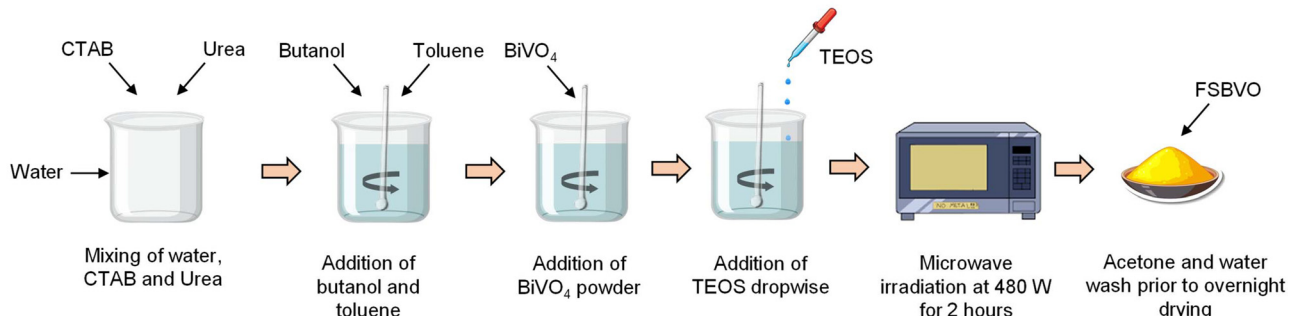
**2.2.2 Deposition of photoanode materials.** The fabricated FSBVO photoanode was deposited on a fluorine-doped tin

oxide (FTO)-coated glass substrate (1 cm × 1 cm) using the carbon paint method, as described in a previous study.<sup>33</sup> The photoanode was initially pre-dried on a hot plate at 50 °C for 10 min, followed by overnight drying in a desiccator. An identical procedure was applied for the preparation of the commercial  $\text{BiVO}_4$  photoanode.

### 2.3 Characterization of the catalyst and photoanode

The phase and crystallinity of the synthesized catalysts were analyzed using X-ray diffraction (XRD) spectroscopy with a Bruker Avance D8 diffractometer (USA) in the  $2\theta$  range of 3° to 90°. The functional groups present in the catalysts were identified through Fourier transform infrared (FTIR) spectroscopy (Agilent Cary 640), employing the KBr pellet method in the spectral range of 1600–400  $\text{cm}^{-1}$ . The surface morphology of the catalysts was examined using field-emission scanning electron microscopy (FESEM) with a JEOL JSM-6701F instrument. The internal microstructure of the catalysts was examined using transmission electron microscopy (TEM, JEM-ARM200F). The bandgap energies were determined through ultraviolet-visible diffuse reflectance spectroscopy (UV-Vis/DRS, Agilent Cary 60), and the corresponding values were extrapolated using a Kubelka–Munk (K–M) plot. The charge carrier densities and flat-band potentials were evaluated *via* Mott–Schottky analysis conducted at a frequency of 1 kHz.

#### Synthesis of fibrous silica bismuth vanadate (FSBVO)



#### Preparation of the photoanode materials

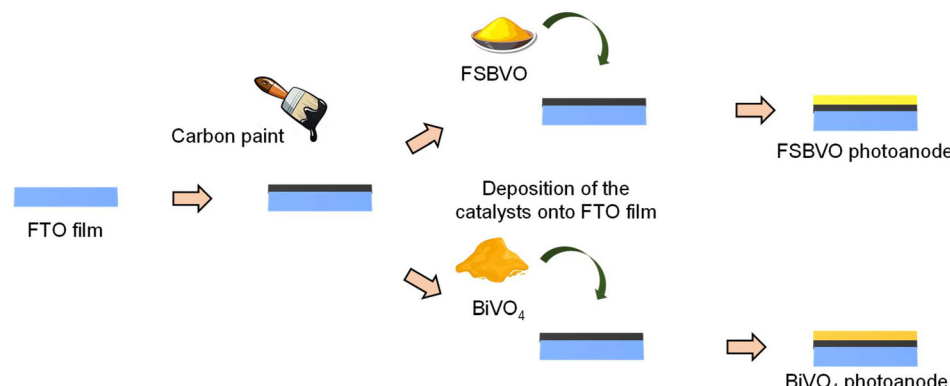


**Fig. 1** Schematic of the preparation of FSBVO and deposition of photoanode materials.

Electrochemical impedance spectroscopy (EIS) was employed to investigate the charge transfer resistance in the photoanode, using a potentiostat (PGSTAT128N, Metrohm Autolab) equipped with a 350 W xenon lamp and an AM 1.5 filter. EIS measurements were performed with a sinusoidal perturbation of 10 mV in the frequency range of 0.1 Hz to 100 kHz. The charge recombination rate of the catalysts was analyzed using photoluminescence (PL) spectroscopy with a fluorescence spectrophotometer (PTI QuantaMaster™ 60, USA). X-ray photoelectron spectroscopy (XPS) was employed to evaluate the chemical oxidation state and electron dynamics in the catalysts (ULVAC-PHI, Japan, PHI5000 Versa Probe II).

#### 2.4 Photoelectrochemical (PEC) measurements

The photoelectrochemical (PEC) water-splitting efficiency of the working electrodes was evaluated using a potentiostat (PGSTAT128N, Metrohm Autolab) paired with a 350 W xenon lamp and an AM 1.5 filter in a three-electrode configuration. The synthesized photoanodes served as the working electrodes, with an Ag/AgCl reference electrode and a platinum counter electrode, operating in a 0.5 M Na<sub>2</sub>SO<sub>4</sub> electrolyte solution at pH 7. Current measurements were performed under both dark and illuminated conditions at a scan rate of 0.01 V s<sup>-1</sup>, applying an external bias of up to 1.5 V vs. Ag/AgCl. The potential data referenced to Ag/AgCl was converted to the reversible hydrogen electrode (RHE) scale using the following conversion equation:

$$E_{\text{RHE}} = E_{\text{Ag/AgCl}} + 0.0591\text{pH} + 0.1976 \quad (1)$$

## 3.0 Results and discussion

### 3.1 Characterization

All photoanode materials were subjected to comprehensive characterization analyses to evaluate their physicochemical, electrochemical, and optical properties, which are critical determinants of their performance in water-splitting reactions.

**3.1.1 Crystallinity and phase studies.** The crystallinity and phase structure of the catalyst were examined *via* XRD analysis. Fig. 2 presents the XRD diffractograms for both the commercial BiVO<sub>4</sub> and the synthesized FSBVO catalysts at  $2\theta = 10^\circ$ – $70^\circ$ . As clearly shown in Fig. 2A, the commercial BiVO<sub>4</sub> exhibits distinct peaks at  $2\theta$  values of  $18.9^\circ$ ,  $28.9^\circ$ ,  $30.6^\circ$ ,  $35.2^\circ$ ,  $39.2^\circ$ ,  $42.5^\circ$ ,  $47.2^\circ$ ,  $50.3^\circ$ ,  $53.3^\circ$ ,  $59.2^\circ$  and  $60.0^\circ$ , corresponding to the crystal planes of (110), (121), (040), (200), (211), (015), (240), (042), (161), (321) and (123), respectively. These peaks are attributed to the monoclinic structure of BiVO<sub>4</sub> and well match the reported JCPDS data no. 14-0688.<sup>35</sup> Conversely, after synthesizing the FSBVO catalyst, a new broad peak at  $2\theta = 22.7^\circ$  appeared prominently, as shown in Fig. 2B, which is likely associated with the amorphous silica structure. This result confirms that silica was successfully introduced in BiVO<sub>4</sub> and suggests that the FSBVO catalyst was effectively synthesized.<sup>36</sup> Notably, analogous peaks attributed to the intrinsic crystal structure of BiVO<sub>4</sub> remained present in FSBVO, with only a slight reduction in intensity, suggesting that the addition of silica did not substantially affect the crystallinity or defect sites of BiVO<sub>4</sub>. Additionally, a distinct peak corresponding to the (101) crystal plane of the orthorhombic V<sub>2</sub>O<sub>5</sub> structure was observed at  $2\theta = 23.5^\circ$ , indicating partial substitution of V species in the Bi–O–V interactions with Si species, leading to the formation of Si–O–Bi vibration.<sup>37</sup> Compared to the other fibrous silica-based developments, the intensity of the peak of silica for the FSBVO catalyst in this study is exceptionally low, which is probably due to the high crystallinity of BiVO<sub>4</sub>.<sup>38,39</sup>

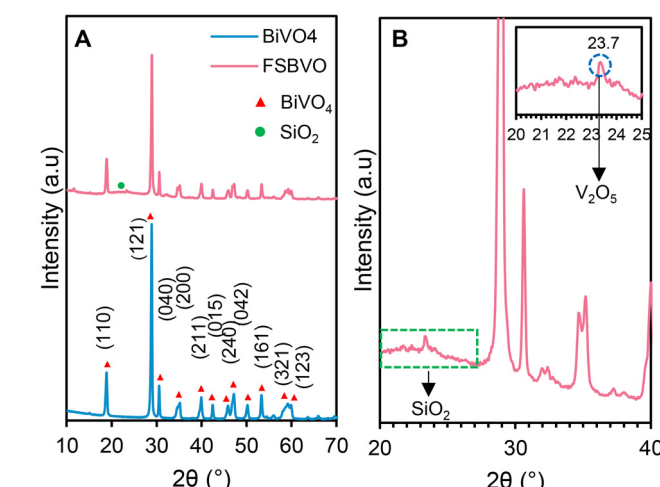


Fig. 2 (A) XRD diffractograms of BiVO<sub>4</sub> and FSBVO catalysts and (B) low-angle XRD diffractogram of FSBVO catalyst in the range of  $2\theta = 20$ – $40^\circ$ .

3.1.2 Functional group studies. Further analysis was conducted using FTIR to determine the functional group present in the catalysts (Fig. 3). Explicitly, the commercial BiVO<sub>4</sub> demonstrated several characteristic peaks in the range of 400–1200 cm<sup>-1</sup>. A weak peak confirming the presence of Bi–O

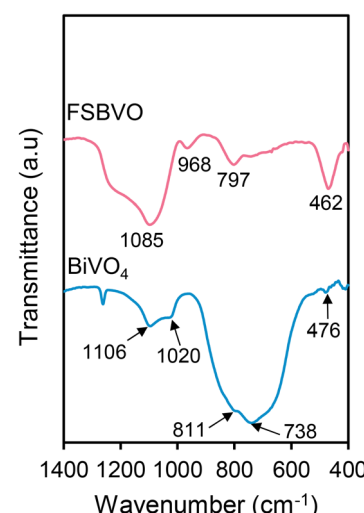


Fig. 3 FTIR spectra of BiVO<sub>4</sub> and FSBVO catalysts.

interaction was detected at  $476\text{ cm}^{-1}$ , which is assigned to the Bi–O bending mode.<sup>40</sup> Furthermore, prominent vibrational signals corresponding to the structural vibration modes of V–O–V species were identified at  $738\text{ cm}^{-1}$  and  $811\text{ cm}^{-1}$ . These peaks are attributed to the asymmetric and symmetric stretching vibrations of  $\text{VO}_4^{3-}$ , respectively.<sup>41–43</sup> Alternatively, clearly defined bands were also observed at  $1020$  and  $1106\text{ cm}^{-1}$ , which are associated with the V–O stretching vibrations within the  $\text{VO}_4^{3-}$  tetrahedral structure.<sup>40</sup> Furthermore, the incorporation of the fibrous silica matrix in  $\text{BiVO}_4$  resulted in the appearance of additional peaks at  $462$ ,  $797$ ,  $968$ , and  $1085\text{ cm}^{-1}$ , which exposed the existence of Si–O–Si bending, Si–O–Si symmetric, Si–OH, and Si–O–Si, respectively.<sup>34,44</sup> The presence of Si–O–Si and Si–OH interactions indicates the formation of an interconnected silica framework, suggesting that silicon and oxygen atoms are now arranged in a well-linked structure. These interconnected silica networks are anticipated to enhance the chemical stability, improve the accessibility of active sites, and thereby extend the lifespan of the catalyst, while optimizing its performance in photoelectrochemical applications.<sup>33</sup> Furthermore, it is noteworthy that the peak associated with the Si–Bi and Si–V interactions is barely detectable in the FSBVO catalyst, which is possibly caused by the low concentration of Bi and V species in FSBVO compared to Si.

In summary, the FTIR analysis offers essential information regarding the molecular composition, bonding characteristics, and structural properties of both the  $\text{BiVO}_4$  and FSBVO catalysts. By determining the specific functional groups and vibrational modes, FTIR deepened our understanding of the chemical interactions and attributes of these materials. This insight is crucial for designing and optimizing photoanodes to improve their performance in solar-driven hydrogen production and other renewable energy technologies.

**3.1.3 Surface morphology studies.** The surface morphology study was conducted to observe the formation of the spherical fibrous morphology, which indicates the successful fabrication of the FSBVO catalyst. The surface and internal surface morphology of the commercial  $\text{BiVO}_4$  and prepared FSBVO were investigated using FESEM and TEM analyses, respectively. As depicted in Fig. 4A, the FESEM image of commercial  $\text{BiVO}_4$  showed stacked small crystals with a smooth surface, which is comparable to a previous study.<sup>45</sup> Upon incorporating silica

species *via* the microemulsion method, the synthesized FSBVO catalyst developed a spherical shape with a distinctive dendrimeric fiber silica structure (Fig. 4B). An analysis of the projected area of approximately 100 particles observed in the FESEM image indicated that the FSBVO catalyst has an average particle size in the range of 300 to 400 nm (Fig. S1†). This result aligns closely with findings reported for other fibrous silica-based materials, confirming the successful synthesis of FSBVO using the microemulsion method.<sup>46,47</sup> Furthermore, elemental mapping and FESEM-EDX analyses were conducted on the FSBVO catalyst to investigate its elemental distribution and composition, respectively. As shown in Fig. S2,† Bi and V were uniformly distributed across the fibrous silica, suggesting that the fibrous and spherical morphology promoted effective metal dispersion. Furthermore, the FESEM-EDX analysis (Fig. S3†) revealed that the FSBVO catalyst predominantly consisted of elemental silicon (Si), together with oxygen (O), vanadium (V), and bismuth (Bi). The significant presence of V species highlights its critical role in improving the water-splitting efficiency of the bismuth-based photoanode.

The TEM analysis was performed to further validate the successful fabrication of the FSBVO catalyst. As illustrated in Fig. 4C, the TEM image of FSBVO revealed a spherical morphology featuring a distinctive dendrimeric structure, which is associated with the silica matrix, aligning well with the aforementioned FESEM observations. This silica matrix is anticipated to enhance the accessibility to the active sites, potentially boosting the water oxidation kinetics of  $\text{BiVO}_4$ . Moreover, some dark spots with a size on the nanoscale were also observed in the TEM image, which can be attributed to the  $\text{BiVO}_4$  species, indicating the formation of  $\text{BiVO}_4$  during the microemulsion synthesis and indirectly additional evidence of the effective integration between the silica matrix and  $\text{BiVO}_4$ .

**3.1.4 Optical and electrochemical property studies.** Ultraviolet-visible diffuse reflectance spectroscopy (UV-Vis/DRS) was performed to evaluate the bandgap energies of the catalysts using the Kubelka–Munk plot, as described by eqn (2).

$$(ahv)^2 = A(hv - E_g) \quad (2)$$

In this equation,  $E_g$  represents the bandgap energy,  $\nu$  is the frequency of light,  $A$  denotes the absorbance ( $\text{cm}^{-1}$ ), and  $h$  is

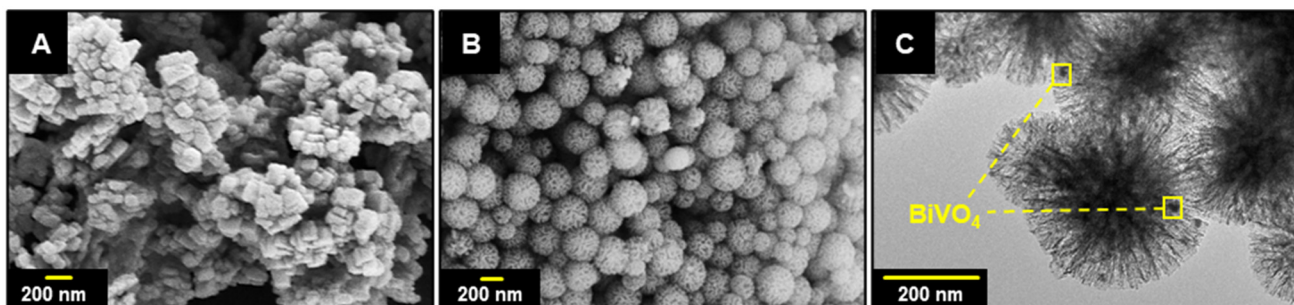
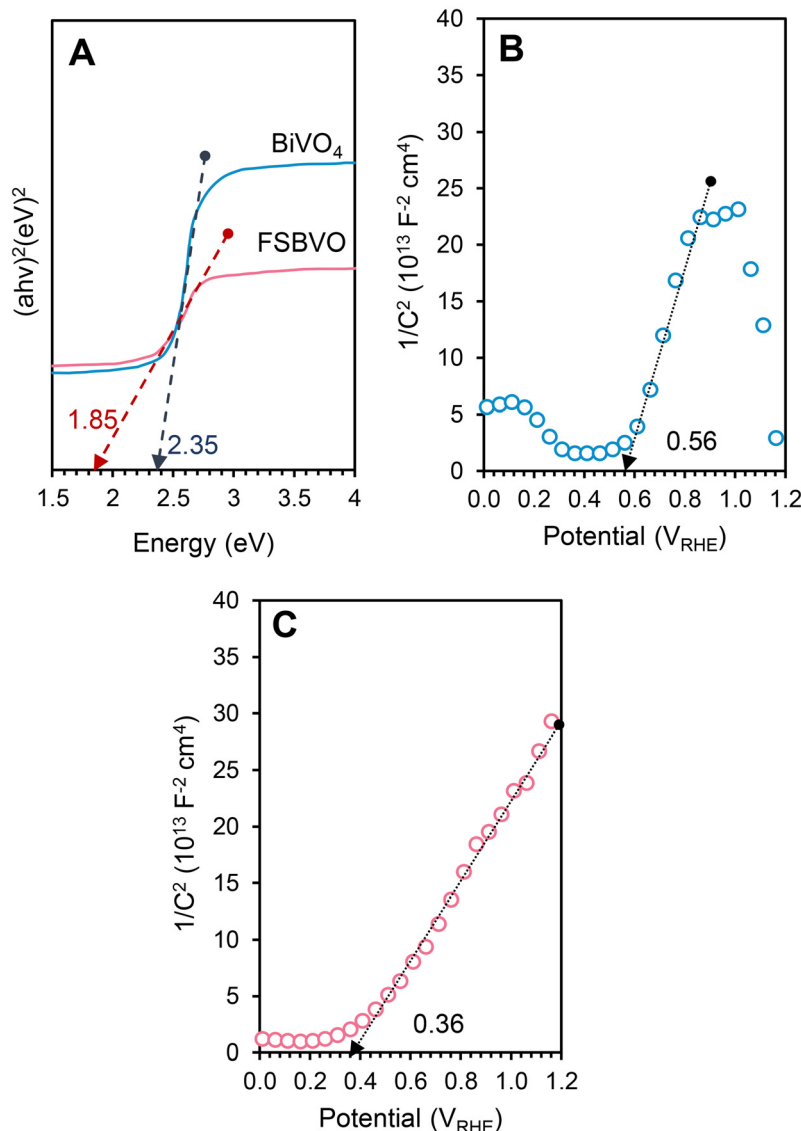


Fig. 4 FESEM images of (A) commercial  $\text{BiVO}_4$  and (B) FSBVO and (C) HRTEM image of FSBVO.



**Fig. 5** (A) Plot of transformed Kubelka–Munk function *versus* the energy of light of  $\text{BiVO}_4$  and FSBVO catalyst. Mott–Schottky plot for (B)  $\text{BiVO}_4$  and (C) FSBVO photoanodes.

the Planck constant. As depicted in Fig. 5A, the commercial  $\text{BiVO}_4$  catalyst exhibited a bandgap energy of 2.30 eV, which is comparable to the values reported in the literature, underscoring its potential as an effective material for visible-light absorption.<sup>48–50</sup> In contrast, the incorporation of a fibrous silica matrix induced a red shift in the bandgap energy of  $\text{BiVO}_4$ . This shift is likely attributed to the unique interactions between  $\text{BiVO}_4$  and silicon, which may introduce defect sites.<sup>34,51</sup> Supporting evidence for this interaction is provided by the reduced intensity of the XRD peaks of  $\text{BiVO}_4$  following the fabrication of the FSBVO catalyst. These interactions are anticipated to enhance the electronic and physicochemical properties of FSBVO, ultimately facilitating efficient charge transfer and a superior PEC water-splitting performance.

Furthermore, the charge transport properties, including carrier density and flat band potential, were evaluated using Mott–Schottky analyses. The results were plotted as space charge capacitance *versus* applied potential, as shown in Fig. 5B and C. Accordingly, the fitting results revealed that both  $\text{BiVO}_4$  and FSBVO displayed positive slopes, indicating that the addition of silica did not affect the n-type semiconductor characteristics of  $\text{BiVO}_4$ , with electrons remaining the primary charge carriers.<sup>38</sup> The flat band potential ( $E_{\text{fb}}$ ) values for the  $\text{BiVO}_4$  and FSBVO photoanodes were extracted by finding the tangent of the slope to the x-intercept. The FSBVO photoanode exhibited an anodic shift in the flat band potential (0.36  $V_{\text{RHE}}$ ) compared to the commercial  $\text{BiVO}_4$  (0.56  $V_{\text{RHE}}$ ), indicating surface state modification. Additionally, the surface charge properties of both photoanodes were analyzed

by applying the Mott–Schottky equations, as expressed in eqn (3) and (4), to calculate the charge carrier density,<sup>52,53</sup> as follows:

$$\frac{1}{C^2} = \frac{2}{N_D A^2 e \epsilon \epsilon_0} \left[ (E - E_{fb}) - \frac{kT}{e} \right] \quad (3)$$

$$\text{slope} = \frac{2}{N_D A^2 e \epsilon \epsilon_0} \quad (4)$$

where  $C$  = space charge capacitance,  $N_D$  = charge carrier density,  $A$  = exposed surface area ( $1 \text{ cm}^2$ ),  $e$  = fundamental electron charges ( $1.60218 \times 10^{-19} \text{ C}$ ),  $\epsilon_0$  = relative permittivity of vacuum ( $8.86 \times 10^{-12} \text{ F m}^{-1}$ ),  $\epsilon$  = relative permittivity of the catalyst ( $\text{BiVO}_4 = 86$  and  $\text{FSBVO} = 12.1$ ),  $E$  = applied potential (V),  $E_{fb}$  = flat band potential,  $k$  = Boltzmann constant ( $1.38065 \times 10^{-23} \text{ J K}^{-1}$ ) and  $T$  = absolute temperature (K).<sup>54,55</sup> Using the aforementioned equation, the charge carrier density of FSBVO was calculated to be  $32.66 \times 10^{26} \text{ cm}^{-3}$ , which was significantly higher than that of the commercial  $\text{BiVO}_4$  ( $1.99 \times 10^{26} \text{ cm}^{-3}$ ). The significant increase in carrier density suggests an improvement in electronic conductivity, which is beneficial for the hydrogen evolution reaction. This enhanced carrier density shifts the Fermi level closer to the conduction band, facilitating more efficient charge transfer and separation at the FSBVO

photoanode/electrolyte interface, which may play a dominant role in contributing to a superior PEC water-splitting performance.<sup>33,56</sup> For clarity, the optical and photoelectrochemical results are summarized in Table 1.

To examine the transfer dynamics of photogenerated charge carriers, EIS analysis was carried out for both the commercial  $\text{BiVO}_4$  and FSBVO photoanodes. In general, a smaller semicircular arc in the EIS Nyquist plots signifies enhanced charge transport at the photoanode interface, reflecting the reduced intrinsic impedance of the material.<sup>57–59</sup> As shown in Fig. 6A, the arc diameter for the FSBVO photoanode is approximately 4.5-times smaller than that of the pristine  $\text{BiVO}_4$ , indicating lower resistance and faster interfacial charge transfer. The notable improvement in charge transfer efficiency for FSBVO can be attributed to the uniform dispersion of  $\text{BiVO}_4$  nanoparticles within the fibrous silica matrix, as well as the synergistic interaction between Bi and Si species, which facilitates efficient charge transfer and separation. Moreover, the equivalent circuit models were plotted based on these results, as shown in Fig. S4.† The bare  $\text{BiVO}_4$  photoanode demonstrated larger impedance values ( $R_s = 25.82 \Omega$  and  $R_{ct} = 962.68 \Omega$ ) compared to the FSBVO photoanode ( $R_s = 24.58 \Omega$  and  $R_{ct} = 334.56 \Omega$ ) (Table 1), which further supported the reduction of impedance achieved by the FSBVO photoanode.

PL analysis was performed to assess the efficiency of electron–hole pair separation in the catalysts. The charge carrier recombination rate is typically inferred from the intensity of the PL emission, where a higher intensity suggests a higher recombination rate and a lower intensity indicates more efficient charge separation.<sup>60,61</sup> As illustrated in Fig. 6B, the PL intensity of FSBVO is marginally lower compared to that of the commercial  $\text{BiVO}_4$ , indicating enhanced electron–hole separation in FSBVO. Similar trends have also been observed in studies involving other fibrous silica-based materials. For instance, Hitam *et al.* and Hassan *et al.* reported significant

**Table 1** Optical and photoelectrochemical properties of  $\text{BiVO}_4$  and FSBVO photoanodes

Photoanode	Bandgap <sup>a</sup> (eV)	$N_D (\times 10^{26} \text{ cm}^{-3})$	$E_{fb}$ (VRHE)	$R_s$ ( $\Omega$ )	$R_{ct}$ ( $\Omega$ )
$\text{BiVO}_4$	2.35	1.99	0.56	25.82	962.68
FSBVO	1.85	32.66	0.36	24.58	334.56

$N_D$ : carrier density.  $E_{fb}$ : flat band potential. <sup>a</sup> Bandgap calculated using Kubelka–Munk (K–M) plot.

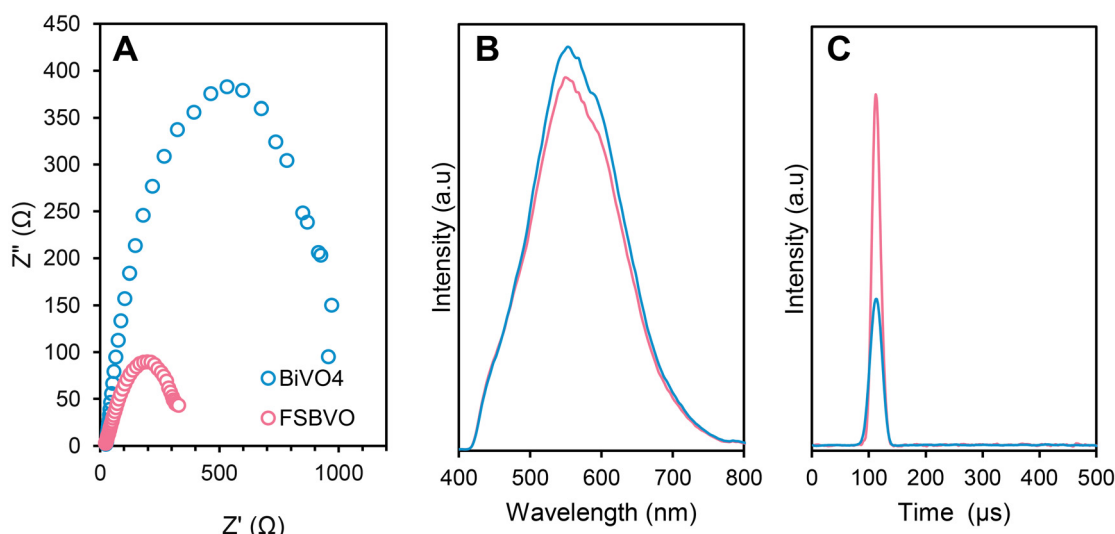


**Fig. 6** (A) EIS Nyquist plot, (B) PL spectra and (C) TRPL spectra of commercial  $\text{BiVO}_4$  and FSBVO.

reductions in the PL intensity for zinc and tantalum catalysts, respectively, upon the incorporation of a silica matrix.<sup>62,63</sup> Moreover, time-resolved photoluminescence (TRPL) decay spectroscopy analysis was conducted to further observe the charge carrier behavior. As depicted in Fig. 6C, FSBVO demonstrated a higher intensity spectrum compared to BiVO<sub>4</sub>. The higher intensity of FSBVO in the TRPL analysis showed that the recombination of charge carriers was significantly suppressed, and ultimately this result supported the observation in the EIS and PL analyses. Consequently, these findings unveil the potential of fibrous silica material to facilitate carrier separation and transfer, which is expected to contribute to the superior water-splitting performance of the FSBVO photoanode.

**3.1.5 Chemical oxidation state analysis.** The surface chemical composition of the FSBVO catalyst was determined by XPS, with the binding energies of all the elements calibrated against the C 1s peak. According to the fine XPS full spectra

displayed in Fig. 7A, the typical signals of Si 2p, O 1s, Bi 4f, and V 2p can be observed, which are consistent with the previously mentioned FESEM elemental mapping result. Deconvolution of the Si 2p spectrum (Fig. 7B) identified two distinct peaks at 100.7 and 101.4 eV, which are likely associated with the Si–O–Si and Si–O–Bi species, respectively.<sup>32</sup> Previous research indicates that the binding energy of Si 2p in pure silica is approximately 103.0 eV.<sup>64</sup> However, in this study, the peaks associated with Si 2p slightly shifted to a low binding energy value, which was possibly due to the migration of adjacent electrons to the silica species. This electron migration caused a notable shielding effect, weakening the interaction between the nucleus and valence electrons.<sup>65,66</sup> Similar phenomena were also reported by Hassan *et al.* and Sawal *et al.* in their studies.<sup>32,67</sup> The shift in the binding energy highlights the presence of interfacial contact between the Si and Bi species, which is consistent with the FTIR results.

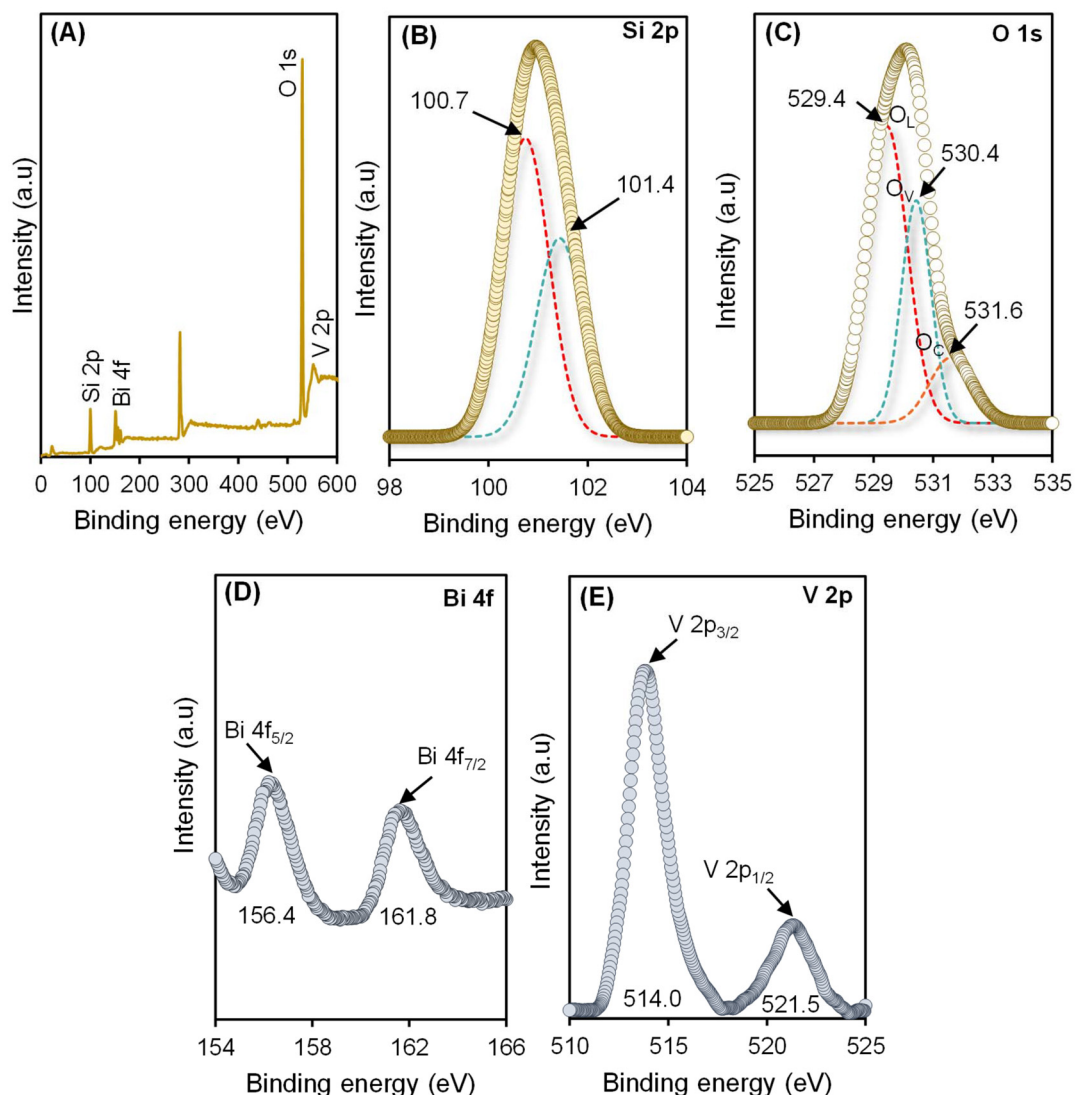


**Fig. 7** XPS (A) survey spectra and (B) Si 2p, (C) O 1s, (D) Bi 4f and (E) V 2p spectra for the FSBVO photoanode.

It is worth noting that the deconvoluted O 1s spectrum (Fig. 7C) revealed three peaks at 529.4, 530.4, and 531.6 eV, corresponding to lattice oxygen ( $O_L$ ), oxygen vacancies ( $O_V$ ), and chemisorbed oxygen ( $O_C$ ), respectively.<sup>68</sup> Additionally, two well-defined peaks at binding energies of 161.8 and 156.4 eV were observed in the Bi 4f spectrum (Fig. 7D), representing the characteristic  $Bi^{3+}$  peaks for  $Bi\ 4f_{5/2}$  and  $Bi\ 4f_{7/2}$ , respectively. Meanwhile, the high-resolution XPS spectrum of V 2p (Fig. 7E) exhibited the typical doublet peaks at 514.0 eV ( $V\ 2p_{3/2}$ ) and 521.5 eV ( $V\ 2p_{1/2}$ ), corresponding to  $V^{5+}$  cations in the monoclinic  $BiVO_4$  phase. Compared to the XPS spectra reported for pristine  $BiVO_4$  in the literature, both the Bi 4f and V 2p signals of the FSBVO catalyst displayed a significant blue shift.<sup>21,69,70</sup> This discovery was most likely caused by the reduction of the electron cloud density surrounding  $BiVO_4$  species upon the fabrication of the FSBVO catalyst, which in turn, provides supplementary evidence of the movement of electrons from  $BiVO_4$

species to the fibrous silica framework.<sup>71,72</sup> Accordingly, these findings highlight the primary role of  $BiVO_4$  species as a light sensitizer material for the generation of more charge carriers. These electrons were later transferred to the Si species, allowing a lower recombination rate for photogenerated carriers, which is consistent with the PL analysis. Overall, the XPS analysis provides essential insights into the surface chemical oxidation states of the catalyst, offering a deeper understanding of the underlying mechanisms for the PEC water-splitting reaction on the FSBVO photoanode.

### 3.2 PEC water-splitting performance

To assess the PEC water-splitting performance, a three-electrode cell evaluation was performed in a 0.5 M  $Na_2SO_4$  electrolyte ( $pH = 7$ ) under AM 1.5 G illumination. As shown in Fig. 8A, the synthesized FSBVO photoanode exhibited a photocurrent density of  $19.8\text{ mA cm}^{-2}$  at  $1.23\text{ V}_{RHE}$ , which is 27.5

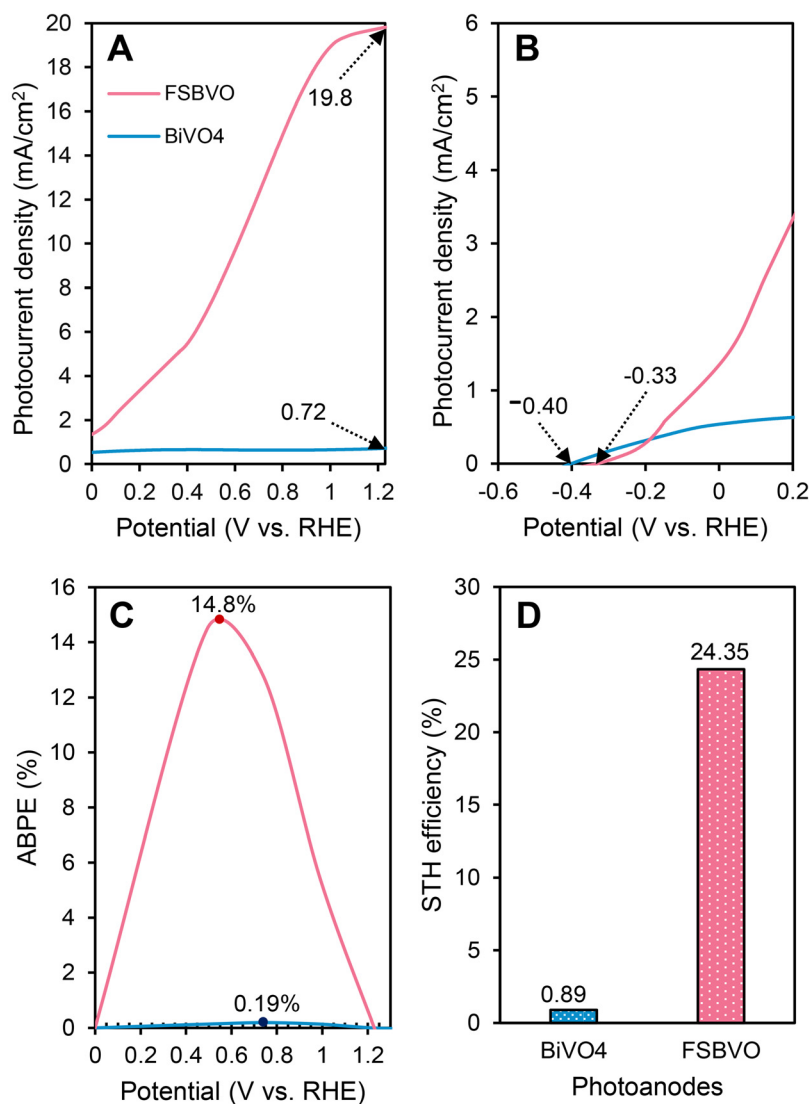


**Fig. 8** (A) Linear sweep voltammetry, (B) onset potential, (C) applied bias-to-photon efficiency and (D) solar-to-hydrogen efficiency of  $BiVO_4$  and FSBVO photoanodes.

times higher than that obtained by the commercial  $\text{BiVO}_4$  ( $0.72 \text{ mA cm}^{-2}$ ). It is worth noting that commercial silica is known for its insulator behavior due to its large bandgap (7.62–9.70 eV), and thus its introduction as a metal oxide support might negatively affect photo-based reactions.<sup>73</sup> Surprisingly, in this study, the addition of the modified silica framework with a tuned bandgap to  $\text{BiVO}_4$  obviously contradicts the conventional reports. One of the possible reasons for this astonishing result might be associated with the unique fibrous silica morphology, which prevents the agglomeration of the  $\text{BiVO}_4$  and promotes the formation of nano-sized  $\text{BiVO}_4$  species (Fig. 4A–C). The unique nano-confinement of  $\text{BiVO}_4$  helps in improving the light absorption capacity, boosting the carrier density (Table 1) and enhancing the charge carrier transport (shown in EIS results). Besides, the unique nano-material also provides more accessibility to the active sites and reduces the carrier recombination, thereby resulting in a high photocurrent density value.<sup>74,75</sup> Similarly, Sabino *et al.* and Azam *et al.* observed a consistent phenomenon over  $\text{TiO}_2$ -based nanoparticles.<sup>76,77</sup> This observation marked the astonishing property of nanoparticles in improving the light absorption efficiency.

Moreover, the presence of the unique Si–Bi interaction was also noted to play a pivotal role in promoting a smooth OER kinetic. This promising interaction substantially reduced the intrinsic impedance (Fig. 6A), and also helped in assisting electron migration (shown by XPS in Fig. 7), in turn enhancing the PEC water-splitting performance. Unlike commercial silica, the bandgap of pristine fibrous silica is about 3.75 eV.<sup>34</sup> Thus, the introduction of fibrous silica in  $\text{BiVO}_4$  seems capable of tuning the original bandgap of  $\text{BiVO}_4$ , resulting in a lower charge recombination rate (shown by PL analysis in Fig. 6B). Interestingly, some comparable findings were also reported for several fibrous silica-based photoanodes. Likewise, Sawal *et al.* reported a photocurrent value of  $13.79 \text{ mA cm}^{-2}$  at  $1.23 \text{ V}_{\text{RHE}}$  achieved by a fibrous silica titania (FST) photoanode.<sup>36</sup> A similar feat was observed by Abdullah *et al.* over a fibrous silica zinc (FSZn) photoanode under the same conditions ( $17.88 \text{ mA cm}^{-2}$ ).<sup>78</sup> In addition, recently, Samia and team fabricated an Ag-doped FST photoanode for a similar application. The fabricated Ag/FST photoanode displayed a comparable photocurrent density ( $13.98 \text{ mA cm}^{-2}$ ) at  $1.23 \text{ V}_{\text{RHE}}$ .<sup>79</sup> These developed fibrous silica-based photoanodes surpassed the theoretical photocurrent density of their respective metal oxides ( $\text{TiO}_2 = 0.55 \text{ mA cm}^{-2}$ ,  $\text{ZnO} = 0.6 \text{ mA cm}^{-2}$ ), which is mainly attributed to the favorable morphology of fibrous silica, unique Si–metal interaction, tunable band edge position and improved of photoelectrochemical properties.<sup>80,81</sup> Consequently, these previous studies supported the astonishing PEC water-splitting performance showcased by the FSBVO photoanode.

Alternatively, the onset potential values for each photoanode were obtained to determine the point at which the electrochemical process started. According to earlier research, the lower the onset potential value, the greater the driving power exerted by the photoanode to activate the electro-

chemical process.<sup>82</sup> As shown in Fig. 8B, the commercial  $\text{BiVO}_4$  had a substantially lower onset potential ( $-0.40 \text{ V}_{\text{RHE}}$ ) than FSBVO ( $-0.33 \text{ V}_{\text{RHE}}$ ), indicating a higher capacity to commence the water-splitting process. The anodic shift of the onset potential of the FSBVO photoanode can be attributed to a portion of the energy being required to overcome the kinetic barrier introduced by the modification of  $\text{BiVO}_4$  with fibrous silica. Interestingly, Jha *et al.* and Wang *et al.* reported comparable occurrences on their modified photoanodes.<sup>83,84</sup> Furthermore, compared with the commercial  $\text{BiVO}_4$ , the photocurrent density of the FSBVO photoanode increased significantly from the onset potential point, indicating that the fabrication of FSBVO *via* the microemulsion method can generate more charge carriers and improve the charge transport and interfacial charge transfer resistance, which eventually led to a higher reaction rate.

Furthermore, the photoconversion efficiency, known as the applied bias photon-to-current conversion efficiency (ABPE), of both the pristine  $\text{BiVO}_4$  and FSBVO photoanodes, was evaluated to assess their water-splitting capabilities and the results are presented in Fig. 8C. Typically, the ABPE values were calculated by subtracting the bias voltage contribution from the LSV curves using the formula provided in eqn (5),<sup>24,85,86</sup> as follows:

$$\text{ABPE} = \frac{J_{\text{ph}} \times (1.23 - V_{\text{app}})}{P_{\text{light}}} \times 100\% \quad (5)$$

where  $J_{\text{ph}}$  is the photocurrent density,  $V_{\text{app}}$  is the applied external potential ( $\text{V}_{\text{RHE}}$ ) and  $P_{\text{light}}$  is the light intensity ( $100 \text{ mW cm}^{-2}$ ). As depicted in Fig. 8C, the bare  $\text{BiVO}_4$  demonstrated a notable low photoconversion efficiency with an ABPE value of 0.19% at  $0.74 \text{ V}_{\text{RHE}}$ . Surprisingly, upon the introduction of the fibrous silica, the photoconversion efficiency of  $\text{BiVO}_4$  was boosted tremendously. The synthetic FSBVO photoanode attained a maximum ABPE of 14.8% at a lower bias ( $0.56 \text{ V}_{\text{RHE}}$ ), which was 77.9-times greater than that of the bare  $\text{BiVO}_4$  and consistent with the aforementioned result shown by the LSV curve. This extraordinary improvement in ABPE can be attributed to the significant enhancement in the physico-chemical and optical properties of FSBVO, which led to efficient artificial solar light utilization.

Additionally, the solar-to-hydrogen (STH) efficiency serves as a crucial metric in PEC water-splitting studies, enabling the evaluation of the effectiveness of photoanodes in converting solar energy into hydrogen fuel. Therefore, the STH efficiencies for both the  $\text{BiVO}_4$  and FSBVO photoanodes were calculated using eqn (6) and the results are illustrated in Fig. 8D.<sup>32,87</sup>

$$\text{STH} (\%) = \frac{J_{\text{p}} (1.23 - V_{\text{app}})}{P} \times 100 \quad (6)$$

where  $J_{\text{p}}$  denotes the photocurrent density at the corresponding applied bias ( $\text{mA cm}^{-2}$ ),  $V_{\text{app}}$  is the applied bias ( $\text{V}_{\text{RHE}}$ ), and  $P$  represents the light intensity ( $100 \text{ mW cm}^{-2}$ ). As noted in Fig. 8D, the commercial  $\text{BiVO}_4$  photoanode displayed an STH efficiency of 0.89%, which is inferior to the theoretical expectation. In contrast, the synthesized FSBVO photoanode

showed a remarkable performance, achieving an STH efficiency of 24.35%, which is 27.4-fold higher than that of the  $\text{BiVO}_4$  photoanode. Notably, this efficiency also surpassed the theoretical efficiency known for commercial  $\text{BiVO}_4$  (9.1%).<sup>88</sup> The substantial enhancement in the STH efficiency of the FSBVO photoanode indirectly highlights the potential of the fibrous silica morphology in improving the properties of photoanode materials to facilitate efficient water-splitting activity.

To further explore the capability of the FSBVO photoanode towards PEC water-splitting, the catalytic activity of  $\text{BiVO}_4$  supported on fibrous silica ( $\text{BiVO}_4@\text{SiO}_2$ ) in the water redox reaction was also investigated. As shown in Fig. S5A,<sup>†</sup> the  $\text{BiVO}_4@\text{SiO}_2$  photoanode demonstrated inferior PEC water-splitting activity compared to the FSBVO photoanode with the photocurrent density at 1.23 V<sub>RHE</sub> of 9.28 and 19.8 mA cm<sup>-2</sup>, respectively. Besides, the onset potential of the  $\text{BiVO}_4@\text{SiO}_2$  photoanode (Fig. S5B<sup>†</sup>) also displayed a slight cathodic shift (-0.24 V<sub>RHE</sub>) compared to the FSBVO photoanode (-0.33 V<sub>RHE</sub>), showcasing the higher driving forces needed by the  $\text{BiVO}_4@\text{SiO}_2$  photoanode to participate in the electrochemical reaction.

As evidenced by the FTIR analysis (Fig. S6A<sup>†</sup>), the  $\text{BiVO}_4@\text{SiO}_2$  photoanode showed a much higher intensity of  $\text{SiO}_2$  functional groups at 1085, 968, 797 and 462 cm<sup>-1</sup> relative to FSBVO, suggesting less Si–Bi interactions in the  $\text{BiVO}_4@\text{SiO}_2$  photoanode, which contributed to the aforementioned findings. In addition, the charge transfer behavior of both photoanodes was compared. As noted in Fig. S6B,<sup>†</sup> the  $\text{BiVO}_4@\text{SiO}_2$  photoanode displayed a substantially larger semi-circle arc compared to the FSBVO photoanode, inferring the presence of significant intrinsic charge impedance. As noted,  $\text{SiO}_2$  exhibited poor electroconductivity. Therefore, owing to the presence of less  $\text{SiO}_2$ –Bi interactions, the overall electron mobility become restricted, which ultimately led to a low PEC water-splitting performance.

Moreover, the  $\text{BiVO}_4@\text{SiO}_2$  photoanode also demonstrated a bandgap energy of 2.30 eV (Fig. S7A<sup>†</sup>), which is higher than that of the FSBVO photoanode (1.85 eV), but slightly lower than that of the commercial  $\text{BiVO}_4$  photoanode (2.35 eV). According to a previous study, the incorporation of metal into fibrous silica *via* the impregnation method usually tends to result in more metal agglomeration compared to the micro-emulsion synthesis route.<sup>34</sup> When this phenomenon occurs, the agglomeration of metal later becomes a bigger crystallite structure, which reduces the penetration of light in the photoanode surface, resulting in a lower light absorption capacity. To support this study, a Mott–Schottky analysis was performed on the  $\text{BiVO}_4@\text{SiO}_2$  photoanode and the results are presented in Fig. S7C,<sup>†</sup> while its electronic properties are summarized in Table S1.<sup>†</sup> It is worth noting that the  $\text{BiVO}_4@\text{SiO}_2$  photoanode exhibited a comparable but slightly lower charge carrier density ( $N_D = 1.14 \times 10^{26} \text{ cm}^{-3}$ ) relative to the commercial  $\text{BiVO}_4$  photoanode ( $N_D = 1.99 \times 10^{26} \text{ cm}^{-3}$ ). However, compared to the FSBVO photoanode ( $N_D = 32.66 \times 10^{26} \text{ cm}^{-3}$ ), the charge carrier density of the  $\text{BiVO}_4@\text{SiO}_2$  photoanode seems

negligible. This observation can be due to the limitation of the exposed surface generating fewer electron–hole pairs, leading to a low charge carrier density. Thus, this indirectly supports the aforementioned UV-Vis/DRS results in Fig. S7A<sup>†</sup> and explains the PEC water-splitting activity behavior shown by the  $\text{BiVO}_4@\text{SiO}_2$  photoanode.

### 3.3 PEC water-splitting mechanism

To investigate the mechanism of the PEC water-splitting reaction on the photoanodes, it was essential to determine their conduction band (CB) and valence band (VB) positions. Specifically, the CB and VB potentials of the photoanodes were calculated using the Mulliken electronegativity concept, as described in the following equations:<sup>89,90</sup>

$$E_{\text{CB}} = X - E_{\text{C}} - 0.5E_{\text{g}} \quad (7)$$

$$E_{\text{VB}} = E_{\text{CB}} + E_{\text{g}} \quad (8)$$

where  $E_{\text{CB}}$  and  $E_{\text{VB}}$  are the conduction and valence band potentials, respectively;  $E_{\text{g}}$  is the bandgap energy of the semiconductor;  $X$  is the absolute electronegativity of the elements, and  $E_{\text{C}}$  refers to the energy of free electrons on the hydrogen scale (4.5 eV).<sup>91,92</sup> Using these equations, the CB potentials of  $\text{BiVO}_4$ ,  $\text{BiVO}_4/\text{SiO}_2$  and FSBVO were calculated to be 0.36, 0.19 and 0.41 eV, respectively. Meanwhile, the calculated VB potentials were 2.71, 2.49 and 2.26 eV, respectively.

Considering the theoretical aspect of the Mulliken electronegativity concept, the band alignments for each photoanode were also compared with the Mott–Schottky method. Based on a previous study, the CB level of the semiconductor lies at 0.1 to 0.3 from the flatband potential.<sup>93,94</sup> By referencing to the Mott–Schottky and UV-Vis/DRS analyses and assuming that the position of the CB is located at 0.2 eV from the flatband potential, the CB for the  $\text{BiVO}_4$ ,  $\text{BiVO}_4@\text{SiO}_2$  and FSBVO photoanodes was calculated to be 0.36, 0.34 and 0.16 eV, respectively. Alternatively, the VB was calculated to be 2.71, 2.64 and 2.01 eV, respectively. It is worth mentioning that the calculated values were only slightly different from the results reported by the Mulliken electronegativity concept, inferring that the Mulliken electronegativity concept is a reliable method for the determination of the band edge of the semiconductors.

Based on the characterization and PEC water-splitting reaction results, the mechanism for the water-splitting reaction over the  $\text{BiVO}_4$  and FSBVO photoanodes was proposed (Fig. 9). When light irradiates the surface of the  $\text{BiVO}_4$  photoanode, electron–hole pairs are generated simultaneously. The illumination of light with a sufficient amount of energy excites the electron in the VB to the CB and produces an electron vacancy known as a hole ( $\text{h}^+$ ). Given that the VB potential of  $\text{BiVO}_4$  exceeds the minimum requirement for water-splitting to occur, the  $\text{h}^+$  generated at the VB of  $\text{BiVO}_4$  will be consumed to split the absorbed water ( $\text{H}_2\text{O}$ ) molecules at the  $\text{BiVO}_4$  surface, producing oxygen molecules ( $\text{O}_2$ ) and protons ( $\text{H}^+$ ). Concurrently, the excited electrons in the CB will directly move to the FTO film and transfer *via* the external circuit to the photocathode,

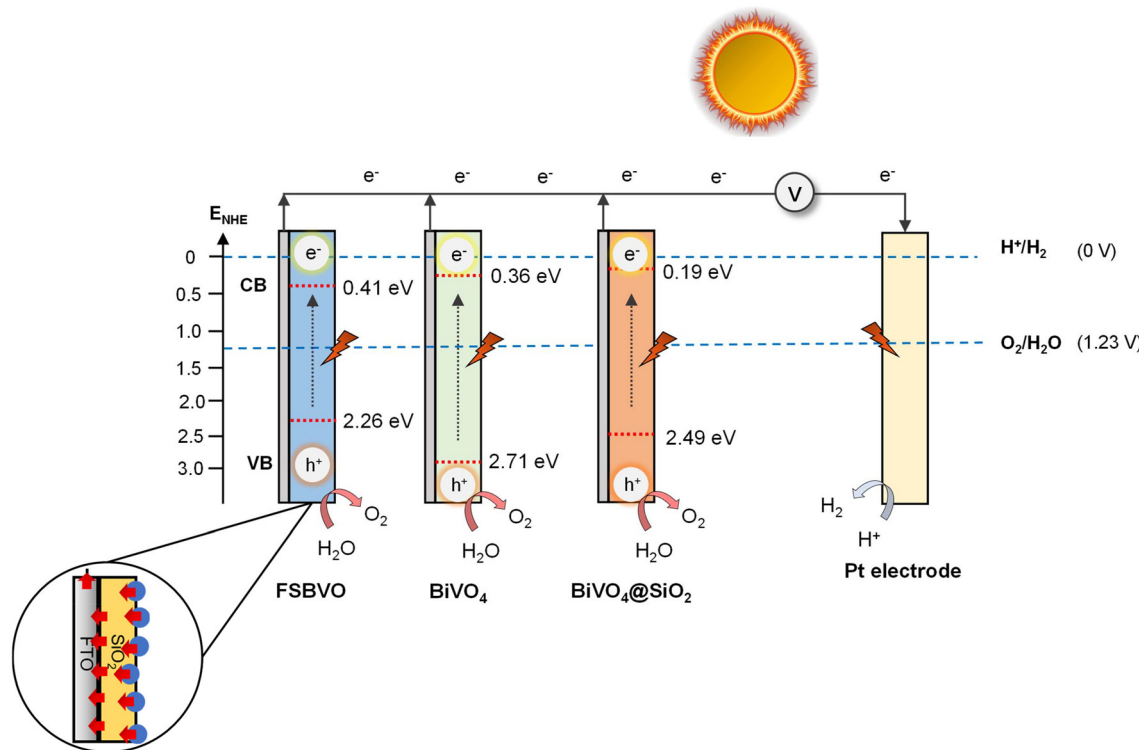


Fig. 9 Proposed mechanism of PEC water splitting over  $\text{BiVO}_4$ -based photoanodes.

where these electrons will be utilized to reduce the free  $\text{H}^+$  in the electrolyte for hydrogen generation.

In contrast, a slight difference in the water-splitting mechanism was proposed over the FSBVO photoanode. After light is irradiated to the FSBVO surface, the electrons will jump from the VB to the CB and produce  $\text{h}^+$ . The  $\text{h}^+$  will be utilized for the oxidation of  $\text{H}_2\text{O}$  to  $\text{O}_2$  and  $\text{H}^+$ , which is similar to that described for the  $\text{BiVO}_4$  photoanode. Nevertheless, as revealed by the XPS analysis (Fig. 7), the excited electrons at the CB of the  $\text{BiVO}_4$  species will firstly migrate to the silica framework before contacting the FTO film and directly supplied to the photocathode *via* an external circuit to undergo a reduction process. As depicted in the FESEM analysis (Fig. 4), the synthesis of the FSBVO catalyst significantly transformed the bulky  $\text{BiVO}_4$  to nanoparticles. This transformation induced a greater light absorption capacity, which is capable of generating more electron-hole pairs ( $N_D = 32.66 \times 10^{26} \text{ cm}^{-3}$ ) and smooth electroconductivity, ultimately leading to a superior PEC water-splitting performance. These observations were supported by the Mott-Schottky analysis and the small semicircle arc in the Nyquist plot, and also aligned well with studies reported by other researchers.

Moreover, the introduction of the fibrous silica morphology facilitated the uniform dispersion of  $\text{BiVO}_4$  and possibly enhanced the accessibility to the active sites. In addition, the silica framework also acts as an electron acceptor (as proven by the XPS analysis in Fig. 7), which reduces the recombination of charge carriers and provides more  $\text{h}^+$  for the oxygen evolution reaction process (OER). Consequently, the substantial

improvement in these physicochemical and electronic properties facilitates smooth charge transfer, ultimately leading to an outstanding water-splitting performance. Likewise, the  $\text{BiVO}_4@\text{SiO}_2$  photoanode displayed a similar mechanism to the FSBVO photoanode. However, despite its unfavourable optical and electrochemical properties, the  $\text{BiVO}_4@\text{SiO}_2$  photoanode also exhibited a VB further from the OER potential level. The position of this VB far from the OER potential level

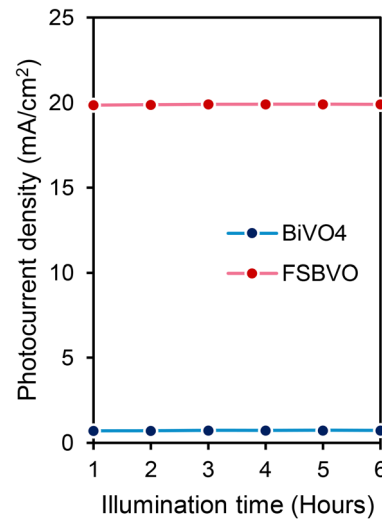


Fig. 10 Long-term stability of the commercial  $\text{BiVO}_4$  and FSBVO photoanodes for PEC water-splitting reaction.

**Table 2** Comparison of PEC water-splitting performance over  $\text{BiVO}_4$  and fibrous silica-based photoanodes

No	Photoanode	Electrolyte	Bandgap (eV)	Photocurrent density ( $\text{mA cm}^{-2}$ at $1.23 \text{ V}_{\text{RHE}}$ )	Ref.
1	$\text{Ni}@\text{NiO}/\text{BiVO}_4$	0.5 M $\text{KPi}$	NA	2.60	95
2	$\text{CoS}/\text{BiVO}_4$	0.5 M $\text{Na}_2\text{SO}_4$	2.40	2.70	96
3	$\text{BiVO}_4/\text{GO}/\text{CoTPP(OH)}_4$	0.5 M $\text{Na}_2\text{SO}_4$	2.51	5.27	99
4	$\text{NiFe-MOFs}/\text{BiVO}_4$	0.5 M $\text{K}_3\text{BO}_3$	2.40	4.61	100
5	$\text{NiFe-O}_{\text{vac}}-\text{BVO}$	0.5 M $\text{K}_3\text{BO}_3$	NA	4.42	97
6	$\text{BiVO}_4/\text{Bi-Cu}$	0.5 M $\text{Na}_2\text{SO}_4$	2.14	10.3	98
7	$\text{Mo-BiVO}_4@\text{rGO}$	0.5 M $\text{Na}_2\text{SO}_4$	2.38	10.3	101
8	FST	0.1 M $\text{Na}_2\text{SO}_4$	2.95	13.8	36
9	FSZn	0.5 M $\text{Na}_2\text{SO}_4$	2.88	17.9	33
10	$\text{Ag}/\text{FST}$	NA	2.40	14.0	79
9	FSBVO	0.5 M $\text{Na}_2\text{SO}_4$	1.85	19.8	This work

NA = not available in the article.

limits the OER process, resulting in a low PEC water-splitting performance.

### 3.4 PEC stability

The stability of a photoanode is a critical factor in assessing its photocorrosion resistance, as well as its potential for commercial-scale applications and overall economic value. The stability test of both the commercial  $\text{BiVO}_4$  and the fabricated FSBVO photoanodes was conducted by prolonging the PEC reaction time to six hours. Fig. 10 illustrates the observed photocurrent density of the photoanodes at  $1.23 \text{ V}_{\text{RHE}}$  for 6 h under constant artificial solar light illumination. As clearly observed in Fig. 10, both the pristine  $\text{BiVO}_4$  and FSBVO photoanodes demonstrated a negligible reduction in photocurrent density during 6 h of illumination. This observation suggests that in addition to improving the PEC water-splitting performance, the incorporation of a fibrous silica framework enhanced or preserved the photocorrosion resistance of the commercial  $\text{BiVO}_4$  in basic electrolyte solution. This enhancement is highly advantageous for scaling up the pilot study to large-scale applications.

The PEC performance of the synthesized FSBVO photoanode was compared to previously reported  $\text{BiVO}_4$ -based photoanodes, and the results are summarized in Table 2. As shown, the PEC performance in this study significantly outperforms that of other  $\text{BiVO}_4$ -based photoanodes reported in the literature. Table 2 highlights that most modified  $\text{BiVO}_4$  photoanodes have bandgap energies in the range of 2.30 to 2.50 eV. In contrast, the FSBVO photoanode exhibits a notably reduced bandgap of 1.85 eV, indicating that the fibrous silica structure effectively broadens its visible light absorption range. Although incorporating metals such as Ni, Co, and Fe has shown limited improvements in photocurrent density, the doping of bimetallic elements such as Bi-Cu on the surface of  $\text{BiVO}_4$  has led to significant enhancements, achieving a photocurrent density of  $10.3 \text{ mA cm}^{-2}$ .<sup>95-98</sup> This finding suggests that choosing an appropriate material is critical for improving the water-splitting performance of photoanodes. Affirmatively, it can be deduced that our findings should provide valuable guidance for the development of advanced and high-performance photoanodes for PEC water splitting.

## 4.0 Conclusion

In conclusion, the FSBVO photoanode was successfully fabricated using the microemulsion method. The physicochemical, optical, and electrochemical properties of the photoanodes were comprehensively analyzed using techniques such as XRD, FTIR, FESEM, TEM, UV-Vis/DRS, Mott-Schottky, EIS, and PL. The FSBVO photoanode demonstrated an exceptional PEC water-splitting performance, achieving a photocurrent density of  $19.8 \text{ mA cm}^{-2}$  at  $1.23 \text{ V}_{\text{RHE}}$ , ABPE of 14.8% at  $0.56 \text{ V}_{\text{RHE}}$ , and STH efficiency of 24.35%. These values are 27.5-, 77.9-, and 27.4-fold higher than that observed for commercial  $\text{BiVO}_4$ , respectively (photocurrent density:  $0.72 \text{ mA cm}^{-2}$ , ABPE: 0.19% at  $0.74 \text{ V}_{\text{RHE}}$ , STH efficiency: 0.89%). The notable improvement in PEC water-splitting performance is attributed to the transformation of the bulky  $\text{BiVO}_4$  species into nanoparticles and the unique fibrous silica framework morphology. These key features enhanced the light absorption, increased the carrier density, facilitated efficient electron transport, and improved the accessibility to the active sites, collectively resulting in notable water-splitting activity. Furthermore, the FSBVO photoanode also exhibited excellent stability under long-term illumination, underscoring its durability and suitability for practical applications. This comprehensive study highlights the critical role of size transformation and material morphology in enhancing the PEC performance of materials. The findings provide valuable insights into the potential of  $\text{BiVO}_4$ -based materials in advancing PEC water-splitting technology and serve as a guide for designing efficient, eco-friendly photoanodes for sustainable energy solutions.

## Author contributions

N. M. Izzudin: conceptualization, resources, formal analysis, visualization, writing draft. A. A. Jalil: writing-review and editing, supervision, project administration, funding acquisition, validation. Saravanan Rajendran: writing-review and editing, conceptualization. N. S. Hassan: writing-review, editing, and conceptualization. M. H. Sawal: data curation,

writing-review, editing, and conceptualization. N. I. H. Hazril: data curation and writing-review. Y. Nagao: writing-review, editing and conceptualization. K. Aoki: writing-review, editing and conceptualization.

## Data availability

The data supporting this article have been included as part of the ESI.†

## Conflicts of interest

The authors declare that they have no known competing financial interests or personal relationships that could have appeared to influence the work reported in this paper.

## Acknowledgements

The authors gratefully acknowledge Universiti Teknologi Malaysia for funding this research work with the Fundamental Research Grant (No. 22H51) and Sakura Science Program (S2023F0200100).

## References

- 1 J. Sun, J. Wang, X. Zhang, Y. Liu, J. Guo, J. Luo, B. Xu and T. Li, *Int. J. Hydrogen Energy*, 2024, **69**, 95–102.
- 2 K. Xue, L. Yu, C. Liu, H. Luo, Z. Li, Y. Zhang and H. Zhu, *J. Colloid Interface Sci.*, 2025, **680**, 771–784.
- 3 Y. Pang, W. Zang, Z. Kou, L. Zhang, G. Xu, J. Lv, X. Gao, Z. Pan, J. Wang and Y. Wu, *Nanoscale*, 2020, **12**, 4302–4308.
- 4 J. Sun, S. Han, F. Yao, R. Li, C. Fang, X. Zhang, Y. Wang, X. Xu, D. Wu, K. Liu, P. Xiong and J. Zhu, *Nanoscale*, 2024, **16**, 4620–4627.
- 5 J. Yang, N. Luo, W. Tang, M. Kuang, C. Tian, H. Chen, H. Yuan and B. Wang, *Int. J. Hydrogen Energy*, 2024, **92**, 580–589.
- 6 W. C. Ng, C. S. Yaw, S. N. A. Shaffee, N. A. A. Samad, Z. K. Koi and M. N. Chong, *Sustainable Mater. Technol.*, 2024, **40**, e00972.
- 7 N. M. Izzudin, A. A. Jalil, S. Rajendran, N. F. Khusnun, N. S. Hassan, M. B. Bahari, M. H. Sawal, M. H. M. Sofi, N. I. H. Hazril and M. Ismail, *J. Electroanal. Chem.*, 2024, **953**, 118011.
- 8 M. S. Tamboli, S. S. Patil, D. K. Lee, C. S. Praveen, A. M. Tamboli, U. Sim, K. Lee, G. H. Gu and C. Park, *Energy*, 2024, **298**, 131329.
- 9 K. Oh, O. De Sagazan, C. Léon, S. Le Gall and G. Loget, *Nanoscale*, 2021, **13**, 1997–2004.
- 10 C. Li, Z. Chen, W. Yuan, Q. H. Xu and C. M. Li, *Nanoscale*, 2019, **11**, 1111–1122.
- 11 L. Zhu, Z. Liang, S. Zhu, Y. Cheng, Z. Li, H. Du, C. Zhu, D. Jiang and Y. Yuan, *Chem. Eng. J.*, 2024, **483**, 149400.
- 12 R. Hu, L. Meng, J. Zhang, X. Wang, S. Wu, Z. Wu, R. Zhou, L. Li, D. S. Li and T. Wu, *Nanoscale*, 2020, **12**, 8875–8882.
- 13 C. Li, S. Li, C. Xu and K. Ma, *Nanoscale*, 2021, **13**, 4654–4659.
- 14 Q. Cai, W. Hong, C. Jian and W. Liu, *Nanoscale*, 2020, **12**, 7550–7556.
- 15 E. Park, S. S. Patil, H. Lee, V. S. Kumbhar and K. Lee, *Nanoscale*, 2021, **13**, 16932–16941.
- 16 Q. Guo, H. Luo, J. Zhang, Q. Ruan, A. P. Periasamy, Y. Fang, Z. Xie, X. Li, X. Wang, J. Tang, J. Briscoe, M. Titirici and A. B. Jorge, *Nanoscale*, 2020, **12**, 20220–20229.
- 17 H. Han, F. Riboni, F. Karlicky, S. Kment, A. Goswami, P. Sudhagar, J. Yoo, L. Wang, O. Tomanec, M. Petr, O. Haderka, C. Terashima, A. Fujishima, P. Schmuki and R. Zboril, *Nanoscale*, 2017, **9**, 134–142.
- 18 S. Fu, D. Lewis, P. van Eyk, P. Atanackovic and Y. Jiao, *Nanoscale*, 2023, **15**, 6913–6919.
- 19 M. G. Guardiano, L. K. Ribeiro, I. M. D. Gonzaga and L. H. Mascaro, *ACS Appl. Nano Mater.*, 2024, **7**, 19569–19578.
- 20 L. Liu, Z. Liu, M. Ruan, Z. Guo and C. Wang, *Catal. Lett.*, 2024, **154**, 4157–4168.
- 21 M. Chen, X. Chang, C. Li, H. Wang and L. Jia, *J. Colloid Interface Sci.*, 2023, **640**, 162–169.
- 22 S. Wang, X. Wang, B. Liu, Z. Guo, K. Ostrikov, L. Wang and W. Huang, *Nanoscale*, 2021, **13**, 17989–18009.
- 23 Y. Hu, Z. Tao, J. Yang, Q. Zhao, J. Li and G. Liu, *J. Alloys Compd.*, 2024, **994**, 174725.
- 24 G. Dong, T. Chen, F. Kou, F. Xie, C. Xiao, J. Liang, C. Lou, J. Zhuang and S. Du, *Nanomaterials*, 2024, **13**(14), 1100.
- 25 N. A. Mohamed, T. S. Kiong, A. F. Ismail and M. A. M. Teridi, *Appl. Surf. Sci.*, 2024, **642**, 158602.
- 26 S. A. Shabbir, M. Haris, R. Ajmal, H. Latif, Q. Abbas, T. Alshahrani, M. M. Al-Anazy, E. S. Yousef, M. Younas and A. Sabah, *Mater. Lett.*, 2024, **360**, 135932.
- 27 A. A. M. Raub, R. Bahru, S. N. A. M. Nashruddin and J. Yunas, *Heliyon*, 2024, **10**, e39079.
- 28 R. Liu, S. Y. Fang, C. Di Dong, K. C. Tsai and W. D. Yang, *Int. J. Hydrogen Energy*, 2021, **46**, 28462–28473.
- 29 C. W. Moon, M. J. Choi, J. K. Hyun and H. W. Jang, *Nanoscale Adv.*, 2021, **3**, 5981–6006.
- 30 A. A. Fauzi, A. A. Jalil, M. Mohamed, S. Triwahyono, N. W. C. Jusoh, A. F. A. Rahman, F. F. A. Aziz, N. S. Hassan, N. F. Khusnun and H. Tanaka, *J. Environ. Manage.*, 2018, **227**, 34–43.
- 31 F. F. A. Aziz, A. A. Jalil, N. S. Hassan, C. N. C. Hitam, A. F. A. Rahman and A. A. Fauzi, *J. Hazard. Mater.*, 2021, **401**, 123277.
- 32 M. H. Sawal, A. A. Jalil, T. A. T. Abdullah, N. F. Khusnun, N. S. Hassan, F. F. A. Aziz, A. A. Fauzi, M. F. A. Kamaruddin, M. F. Omar and S. Haron, *Energy Convers. Manage.*, 2022, **274**, 116456.

33 R. Abdullah, A. A. Jalil, M. Asmadi, N. S. Hassan, M. B. Bahari, N. M. Izzudin, M. H. Sawal, T. A. T. Abdullah, M. A. Aziz, M. Alhassan and S. Rajendran, *J. Electroanal. Chem.*, 2024, **966**, 118385.

34 N. M. Izzudin, A. A. Jalil, M. W. Ali, F. F. A. Aziz, M. S. Azami, N. S. Hassan, A. A. Fauzi, N. Ibrahim, R. Saravanan and M. H. Hassim, *Chemosphere*, 2022, **308**, 136456.

35 M. Rekaby and M. Matar, *J. Mater. Res.*, 2023, **38**, 1543–1556.

36 M. H. Sawal, A. A. Jalil, T. A. T. Abdullah, N. F. Khusnun, N. S. Hassan, F. F. A. Aziz, A. A. Fauzi, M. F. A. Kamaruddin, M. F. Omar and S. Haron, *Energy Convers. Manage.*, 2022, **274**, 116456.

37 K. S. Prasad, C. Shivamallu, G. Shruthi and M. Prasad, *ChemistrySelect*, 2018, **3**, 3860–3865.

38 M. H. Sawal, A. A. Jalil, T. A. T. Abdullah, N. S. Hassan, M. B. Bahari, N. M. Izzudin, N. W. C. Jusoh, Y. Nagao, K. Aoki, M. N. Chong and S. Rajendran, *Int. J. Hydrogen Energy*, 2025, **104**, 336–343.

39 N. I. H. Hazril, A. A. Jalil, F. F. A. Aziz, N. S. Hassan, A. A. Fauzi, N. F. Khusnun, N. M. Izzudin, N. W. C. Jusoh, L. P. Teh, N. F. Jaafar and S. Rajendran, *Sustainable Mater. Technol.*, 2024, **41**, e00994.

40 P. Sharma, V. Virole, T. Anwar, O. Kolekar, A. A. Kale, S. S. Chapadgaonkar and A. Yengantiwar, 2024, **13276**, 132760I.

41 Y. Hu, Z. Tao, J. Yang, Q. Zhao, J. Li and G. Liu, *J. Alloys Compd.*, 2024, **994**, 174725.

42 P. Pookmanee, S. Kojinok, R. Puntharod, S. Sangsrichan and S. Phanichphant, *Ferroelectrics*, 2013, **456**, 45–54.

43 V. G. Warrier, J. Devasia, A. Nizam, V. L. Vasantha, G. Nagaraju and G. Nagendra, *Int. J. Environ. Anal. Chem.*, 2022, 1–20.

44 M. B. Bahari, C. R. Mamat, A. A. Jalil, L. S. Shing, N. S. Hassan, F. F. A. Aziz, M. Alhassan, M. G. M. Nawawi, K. Kidam and H. D. Setiabudi, *Fuel*, 2022, **328**, 125257.

45 J. M. Riega, R. Loyola, M. M. Gomez and J. L. Solis, *J. Phys.: Conf. Ser.*, 2019, **1173**, 012010.

46 M. A. Aziz, A. A. Jalil, N. S. Hassan, M. B. Bahari, T. A. T. Abdullah, N. W. C. Jusoh, Y. Nagao, K. Aoki, S. Nishimura and R. Saravanan.

47 N. S. Hassan, A. A. Jalil, I. C. M. Fei, M. T. A. Razak, N. F. Khusnun, M. B. Bahari, Y. I. Riwayati, S. Suprapto, D. Prasetyoko, M. L. Firmansyah, N. F. M. Salleh and S. Rajendran, *Chemosphere*, 2023, **338**, 139502.

48 D. Wang, H. Wang, J. Fan, H. Zhu, A. Fujishima and X. Zhang, *Int. J. Hydrogen Energy*, 2024, **68**, 596–606.

49 H. Shen, G. Dawson, Y. Wu, F. Cao and X. Cheng, *Chem. Phys.*, 2025, **588**, 2–7.

50 S. Jia, Y. Fang, Z. Liu, K. Tian, X. Zhao and S. Bai, *J. Photochem. Photobiol. A*, 2025, **461**, 116156.

51 N. S. Hassan, A. A. Jalil, C. N. C. Hitam, M. H. Sawal, M. N. S. Rahim, I. Hussain, N. W. C. Jusoh, R. Saravanan and D. Prasetyoko, *Int. J. Hydrogen Energy*, 2023, **48**, 6575–6585.

52 S. F. Lee, E. Jimenez-relinque, I. Martinez and M. Castellote, *Catalysts*, 2023, **13**(6), 1000.

53 S. M. Ho-Kimura, *ACS Appl. Energy Mater.*, 2024, **7**, 1902–1913.

54 K. H. Ye, X. Yu, Z. Qiu, Y. Zhu, X. Lu and Y. Zhang, *RSC Adv.*, 2015, **5**, 34152–34156.

55 H. Sung, S. Ju, C. Park, J. Park, W. Kim, H. Song, S. Lee, S. Son, J. Park and H. Lee, *Sol. Energy Mater. Sol. Cells*, 2024, **274**, 113006.

56 T. Zhang, M. Chen, X. Zhu and P. Lin, *Int. J. Hydrogen Energy*, 2025, **107**, 469–477.

57 Y. Xing, J. Yi, X. Zhang, X. Jin, Y. Peng, G. Ni, X. Yong and X. Wang, *J. Photochem. Photobiol. A*, 2024, **448**, 115322.

58 J. Wu, X. Li, D. Fan, M. Li, H. Zhu and S. Li, *J. Electroanal. Chem.*, 2024, **965**, 118367.

59 Z. Li, Z. Xie, W. Li, H. S. Aziz, M. Abbas, Z. Zheng, Z. Su, P. Fan, S. Chen and G. Liang, *Materials*, 2023, **16**(9), 3414.

60 K. Chen, L. Zhang, X. Huang, F. Zhang, G. Zhu and Q. Wang, *J. Alloys Compd.*, 2023, **963**, 171262.

61 Y. Sun, H. Chen, Z. Hou, J. Wang, A. Li and P. F. Corvini, *Chem. Eng. J.*, 2024, **501**, 157662.

62 C. N. C. Hitam, A. A. Jalil and Y. O. Raji, *Top. Catal.*, 2020, **63**, 1169–1181.

63 N. S. Hassan, A. A. Jalil, C. N. C. Hitam, M. H. Sawal, M. N. S. Rahim, I. Hussain, N. W. C. Jusoh, R. Saravanan and D. Prasetyoko, *Int. J. Hydrogen Energy*, 2023, **48**, 6575–6585.

64 J. Kamalakkannan and S. Senthilvelan, *Can. Chem. Trans.*, 2016, 410–429.

65 B. L. Lin, R. Chen, M. L. Zhu, A. S. She, W. Chen, B. T. Niu, Y. X. Chen and X. M. Lin, *Catalysts*, 2024, **14**(9), 639.

66 P. Arunachalam, M. N. Shaddad, M. S. Amer and A. Al-Qadi, *Alexandria Eng. J.*, 2024, **99**, 64–75.

67 N. S. Hassan, A. A. Jalil, E. M. S. Aldeen, M. Bahari, L. P. Teh, S. Rajendran, N. W. C. Jusoh and N. Ainirazali, *J. Water Process Eng.*, 2024, **59**, 105050.

68 A. Song, Y. Zhang, Z. Li and J. Hu, *Mater. Sci. Eng., B*, 2024, **302**, 117241.

69 M. S. Sudi, L. Zhao, Q. Wang, Y. Dou, X. Shen, A. Wang and W. Zhu, *Appl. Surf. Sci.*, 2022, **606**, 154753.

70 A. Song, Y. Zhang, Z. Li and J. Hu, *Mater. Sci. Eng., B*, 2024, **302**, 117241.

71 H. Song, S. Liu, M. Zhang, W. Wu, R. Qu, C. Zheng and X. Gao, *Energies*, 2018, **11**, 1–13.

72 G. Ma, Y. Xu, J. Wang, J. Bai, Y. Du, J. Zhang and M. Ding, *RSC Adv.*, 2020, **10**, 10723–10730.

73 E. Güler, G. Uğur, Ş. Uğur and M. Güler, *Chin. J. Phys.*, 2020, **65**, 472–480.

74 C. Li, S. Ma, M. Zhao, M. Jing, W. Yuan and C. Li, *ACS Sustainable Chem. Eng.*, 2023, **11**, 12102–12113.

75 M. Mohsin, T. Ishaq, I. A. Bhatti, Maryam, A. Jilani, A. A. Melaibari and N. H. Abu-Hamdeh, *Nanomaterials*, 2023, **13**(3), 546.

76 A. Azam and T. Iqbal, *J. Inorg. Organomet. Polym. Mater.*, 2024, **34**, 5596–5619.

77 F. P. Sabino and A. Janotti, Dramatic enhancement of visible-light absorption in  $TiO_2$  by adding Bi, *arXiv*, 2023, preprint, arXiv:2302.02461, DOI: [10.48550/arXiv.2302.02461](https://doi.org/10.48550/arXiv.2302.02461).

78 R. Abdullah, A. A. Jalil, M. Asmadi, N. S. Hassan, M. B. Bahari, N. M. Izzudin, M. H. Sawal, T. A. T. Abdullah, M. A. Aziz, M. Alhassan and S. Rajendran, *J. Electroanal. Chem.*, 2024, **966**, 118385.

79 S. Arain, M. Usman, F. Saeed, S. Feng, W. Rehman, X. Liu and H. Dai, *Catalysts*, 2025, **15**(1), 66.

80 S. C. Wang, F. Q. Tang and L. Z. Wang, *J. Inorg. Mater.*, 2018, **33**, 173–197.

81 H. A. Mahmoud, K. Narasimharao, T. T. Ali and K. M. S. Khalil, *Nanoscale Res. Lett.*, 2018, **13**, 48.

82 Y. Yao, J. Wu, B. Lv, J. Wei, R. Huang, X. Wang and W. Wang, *Sol. Energy*, 2024, **273**, 112547.

83 Y. Wang, S. Pan, H. Li, D. Li, Y. Guo, S. Chi, C. Geng, S. Wu and Q. H. Yang, *EES Catal.*, 2023, **1**, 312–321.

84 B. K. Jha, S. Chaule and J. H. Jang, *Mater. Chem. Front.*, 2024, **8**, 2197–2226.

85 L. Shuai, L. Tian, X. Huang, J. Dou, J. Yu and X. Chen, *Int. J. Hydrogen Energy*, 2024, **88**, 19–28.

86 N. A. Mohamed, A. F. Ismail, T. S. Kiong and M. A. M. Teridi, *Int. J. Hydrogen Energy*, 2024, **59**, 1063–1079.

87 C. S. Tan, K. W. Kemp, M. R. Braun, A. C. Meng, W. Tan, C. E. D. Chidsey, W. Ma, F. Moghadam and P. C. McIntyre, *Sustainable Energy Fuels*, 2019, **3**, 1490–1500.

88 L. Geronimo, C. G. Ferreira, V. Gacha, D. Raptis, J. Martorell and C. Ros, *ACS Appl. Energy Mater.*, 2024, **7**, 1792–1801.

89 P. Praus, *Carbon*, 2021, **172**, 729–732.

90 J. Gao, W. Zeng, R. Luo, Z. Liu and Q.-J. Liu, *Cryst. Growth Des.*, 2024, **24**, 3777–3785.

91 A. Das, D. Liu, Y. Wu, B. A. Abzakh, R. Madhumitha, M. Preethi, E. A. Kazakova, A. S. Vasenko and O. V. Prezhdo, *J. Phys. Chem. Lett.*, 2024, **15**, 7524–7532.

92 S. A. Shabbir, I. Ali, M. Haris, H. Latif, A. Sabah, A. S. Alshomrany and Y. Bakkour, *ACS Omega*, 2024, **9**, 21450–21458.

93 T. Zhou, J. Wang, S. Chen, J. Bai, J. Li, Y. Zhang, L. Li, L. Xia, M. Rahim, Q. Xu and B. Zhou, *Appl. Catal., B*, 2020, **267**, 118599.

94 S. N. S. Nasir, N. A. Mohamed, M. A. Tukimon, M. F. M. Noh, N. A. Arzaee and M. A. M. Teridi, *Physica B: Condens. Matter*, 2021, **604**, 412719.

95 J. Y. Cui, S. S. Zhu, Y. Zou, Y. Zhang, S. Y. Yuan, T. T. Li, S. Y. Guo, H. Liu and J. J. Wang, *Catalysts*, 2022, **12**(11), 1456.

96 H. She, M. Jiang, P. Yue, J. Huang, L. Wang, J. Li, G. Zhu and Q. Wang, *J. Colloid Interface Sci.*, 2019, **549**, 80–88.

97 Y. Yang, S. Wan, R. Wang, M. Ou, X. Fan and Q. Zhong, *J. Colloid Interface Sci.*, 2023, **629**, 487–495.

98 P. Subramanyam, B. Meena, D. Suryakala and C. Subrahmanyam, *Sol. Energy Mater. Sol. Cells*, 2021, **232**, 111354.

99 A. Wang, X. Shen, J. Ren, Q. Wang, W. Zhao, W. Zhu and D. Shang, *Dyes Pigm.*, 2021, **192**, 109468.

100 Y. Li, Q. Wang, X. Hu, Y. Meng, H. She and L. Wang, *Chem. Eng. J.*, 2022, **433**, 133592.

101 P. Subramanyam, T. Vinodkumar, D. Nepak, M. Deepa and C. Subrahmanyam, *Catal. Today*, 2019, **325**, 73–80.